Journal of Materials Chemistry A

ROYAL SOCIETY OF CHEMISTRY

PAPER

View Article Online
View Journal

Cite this: DOI: 10.1039/d5ta06740e

Recycling with precision: engineering Ni-rich NMC cathodes through impurity management

Xiaochu Wei, [a] Muhammad Ans,[b] Vimalnath Selvaraj,[b] Benjamin Wickham,[b] Christian Marston,[b] Anna Hankin [a] and Maria-Magdalena Titirici *[ac]

The exponential rise in lithium-ion battery (LIB) demand is placing unprecedented pressure on critical metal resources (*e.g.*, Li, Ni, Co), while also generating large volumes of end-of-life battery waste. Although recycling offers a sustainable alternative to virgin mineral extraction, residual impurities introduced during recycling often degrade the performance of resynthesised cathode active materials. In this study, we investigate the structure, morphology and electrochemical properties of $LiNi_{0.8}Mn_{0.1}Co_{0.1}O_2$ (NMC811) cathodes resynthesised from metal salts recovered from spent LIB black mass through an industrial-scale recycling process. The resynthesised cathodes achieved battery-grade purity (99.6%) and exhibited comparable composition and crystal structure to the commercial reference, although morphological deviations were observed due to impurity-induced effects during resynthesis. They delivered an initial discharge capacity of 175.1 mAh g^{-1} with a coulombic efficiency of 92.6% at 0.05C during the first formation cycle, tested in NMC||graphite full cells with an areal loading of 11.3 mg cm^{-2}. At 0.2C, the discharge capacity reached 165.3 mAh g^{-1}, with 95.1% capacity retention after 50 cycles. This study demonstrates the practical feasibility of incorporating recovered precursors into NMC811 cathode production, advancing circularity in LIB manufacturing, while also highlighting that impurity sensitivity during resynthesis remains an important consideration.

Received 19th August 2025
Accepted 4th December 2025

DOI: 10.1039/d5ta06740e

rsc.li/materials-a

Introduction

Lithium-ion batteries are integral to the clean energy transition, serving as the primary power source for electric vehicles (EVs) and grid storage systems. As deployment accelerates, global demand for LIBs has surged dramatically in recent years, driving the need for critical metals such as lithium, cobalt, nickel and manganese. This trend is reflected in recent EU assessments, which project a several-fold increase in demand for these materials by 2030.[1–3] However, the availability of these resources is increasingly constrained by limited natural reserves, geopolitical tensions, and growing competition across industries.[4] Meanwhile, by 2030, over 1.2 million tons of spent LIBs are expected to reach end-of-life, representing both a sustainability challenge and a potential environmental hazard.[5] Recycling is therefore an essential strategy to secure critical materials, reduce dependence on primary mining, and lower environmental impacts.

Among battery components, cathode active materials are the most valuable targets for recycling because of their dominant contribution to battery cost, energy density, and lifespan. Lithium nickel manganese cobalt oxides (NMCs) are widely used for their balance of capacity, stability, and cost-effectiveness, with Ni-rich variants such as NMC622 and NMC811 increasingly adopted to achieve higher specific capacities.[6] However, NMC cathodes are resource- and carbon-intensive, and for NMC811, climate impacts from nickel sourcing can vary by up to 74 kg CO_2eq. per kWh, making it one of the most environmentally burdensome stages in the supply chain.[7] Using recycled precursors avoids this high-impact stage entirely, and industrial-scale life cycle assessments show that producing battery-grade cathode materials from mixed-stream recycled LIBs can reduce overall environmental impacts by at least 58% compared with mining-based supply chains.[8] Reflecting the importance of these sustainability gains, the European Union has introduced Regulation (EU) 2023/1542 on batteries and waste batteries, which includes the battery passport to ensure traceability across the value chain and sets binding minimum recycled content targets by 2031 (16% cobalt, 6% lithium, 6% nickel).[9,10] These assessments and policy measures together underscore the critical role of NMC cathode recovery in building a resilient, traceable, and low-impact battery supply chain.

Most industrial recycling processes rely on hydrometallurgical methods involving leaching, solvent extraction and/or chemical precipitation to recover metals in the form of metal

[a]*Department of Chemical Engineering, Imperial College London, London SW7 2AZ, UK. E-mail: m.titirici@imperial.ac.uk*

[b]*Altilium Clean Technology, Plymouth Science Park, Plymouth, PL6 8BX, UK*

[c]*Advanced Institute for Materials Research (WPI-AIMR), Tohoku University, 2-1-1 Katahira, Aoba-ku, Sendai, Miyagi 980-8577, Japan*

salts.[11] However, these recovered precursors often carry residual impurities originating from other cell components (*e.g.*, current collectors, casings and electrolytes)[5,11–13] or from chemicals used in the recycling process.[14,15] These residual contaminants such as copper (Cu), aluminium (Al), and non-metallic elements can compromise the purity, crystallinity and morphology of the resynthesised NMCs, thereby degrading their electrochemical performance.[14,16–20] For instance, Cu^{2+} and Al^{3+} ions can distort the lattice structure of resynthesised NMC powders, promoting undesired cation mixing that lead to decline in rate capability and cycling stability.[12,21] Non-metallic impurities, such as sulphur, fluorine, and chlorine, although present in lower concentrations relative to metallic species, are also significant, yet less studied.[20] These issues are especially critical for Ni-rich NMCs, which are more susceptible to structural degradation, thermal instability, and moisture sensitivity.[22–24] As a result, managing residual impurities in recovered precursors is critical for meeting the stringent purity and performance standards required for Ni-rich cathodes. While several studies have explored the resynthesis of Ni-rich NMCs from recycled materials,[15,25] no studies to date have evaluated the structural, morphological, and electrochemical characteristics of NMC811 synthesised from industrially recovered metal salts obtained *via* pilot-scale battery recycling. In this work, we present a case study examining these characteristics for NMC811 cathodes resynthesised from such pilot-scale recovered precursors. Elemental analysis of the resynthesised NMC811 identified trace impurities, including sulphur, sodium, and iron. Despite this, the overall purity of NMC811 cathodes remained above 99.6%, consistent with industrial battery-grade specifications. The resynthesised NMC811 cathode exhibited a discharge capacity comparable to that of commercial benchmarks, with excellent coulombic efficiency and enhanced capacity retention in both NMC811‖Li half-cell and NMC811‖graphite full-cell configurations. These results provide valuable insight into the influence of impurities on NMC811 characteristics, particularly with respect to morphology.

Experimental methods

NMC811 material synthesis

All the metal sulphates used for NMC811 resynthesis were recovered from spent LIB black mass through proprietary recycling processes developed by Altilium Clean Technology. For comparison, the commercial sulphates (99.9% purity), including $NiSO_4 \cdot 6H_2O$, $CoSO_4 \cdot 7H_2O$, and $MnSO_4 \cdot H_2O$, were purchased from HD chemicals, UK and served as a control to evaluate the impact of feedstock purity and synthesis conditions.

The $NMC(OH)_2$ precursor, targeting the ideal $LiNi_{0.8}Mn_{0.1}Co_{0.1}O_2$ stoichiometry, was prepared in a 10 L reactor using co-precipitation method, as reported in previous studies employing either recovered or commercial sulphates.[26,27] The sulphates were dissolved in deionised (DI) water and heated to 80 °C for de-aeration. 1.5 M sulphate solution, along with 4 M NaOH and 1 M $NH_4 \cdot OH$ were introduced into the reactor under a continuous N_2 gas flow. The pH was maintained at 11.3, and the reaction temperature at 60 °C, with a stirring rate of 600 rpm. After 20 hours, the resulting hydroxide precursor was filtered, thoroughly washed, and then dried under vacuum at 120 °C overnight.

The dried precursor was then ground and homogenised with a stoichiometric amount of LiOH using an agate mortar and pestle. The resulting mixture was calcined in a tube furnace at 800 °C for 15 hours, with a heating and cooling rate of 5 °C min^{-1}. Finally, the metal oxide powder was mechanically milled to achieve a particle size below 10 μm. The resulting NMC811 samples included NMC-R1 and NMC-R2, both synthesised from recovered sulphates, and NMC-CS, synthesised from commercial sulphates. NMC-R2 underwent an additional impurity removal step developed by Altilium Clean Technology as part of their proprietary recycling process. A commercial NMC811 material purchased from BASF, Germany was used as a benchmark and is referred to as NMC-BASF.

Structural characterisation

All NMC811 samples were subjected to microwave digestion (MARS 6, CEM) using 4 mL of 69 wt% nitric acid (HNO_3) and 2 mL of 37 wt% hydrochloric acid (HCl) per 0.05–0.1 g of sample. The resulting solutions were then analysed by inductively coupled plasma mass spectrometry (ICP-MS 7900, Agilent Technologies) to quantify elemental composition. NMC powder morphology was characterised using scanning electron microscopy (SEM) with a JEOL 6010LA instrument and a Zeiss Sigma instrument for higher magnifications. PXRD measurements of powder samples were performed using a Rigaku MiniFlex600 benchtop X-ray diffractometer with Co Kα radiation, operated at 15 mA and 40 kV. Note that cobalt radiation (λ = 1.788 Å) was used instead of the more common Cu Kα (λ = 1.5406 Å). The incident X-ray beam included a Ni Kβ filter, a 13 mm open X-ray mask and a 2.5° Soller slit. Data collection was performed in goniometer mode using a thin glass sample holder, with a scan speed of 10° min^{-1} over a 3–90° scan range and step width of 0.01°. Rietveld refinement was carried out using GSAS-ll software.[28,29] The tapped density of the NMC811 samples was measured using a Micromeritics GeoPyc 1360, with each value averaged over ten repetitions. The skeletal density was determined using a Micromeritics AccuPyc II 1340 helium pycnometer at ambient temperature under a helium atmosphere, also averaged over ten measurements. The pH of the water extract was measured to assess the surface alkalinity of the powders. A 10 wt% suspension of NMC811 samples in DI water was stirred for 1 h at 25 ± 2 °C in a sealed vessel to minimise CO_2 absorption. The particle size distribution was obtained using a laser diffraction particle size analyser (Anton Paar PSA 1190), with each reported value averaged from three independent measurements. The specific surface area was measured by nitrogen adsorption–desorption using a Micromeritics 3Flex surface characterisation analyser and calculated using the Brunauer–Emmett–Teller (BET) method.

Electrochemical characterisation

Coin cell components (CR2032) and Li metal foil were purchased from Guangdong Canrd New Energy Technology Co.,

Ltd. 1.0 M $LiPF_6$ in ethylene carbonate (EC) and dimethyl carbonate (DMC) electrolyte, sodium carboxymethyl cellulose binder (CMC, $M_w \approx 250\,000$) and Whatman GF/A glass microfiber were purchased from Sigma Aldrich. All chemicals were used as received without further purification.

The slurry for all the NMC811 cathodes were prepared by mixing 90 wt% NMC811 powder with 6 wt% pre-prepared PVDF binder solution (5 wt% in NMP) and 4 wt% carbon black. The slurry for graphite anode was prepared by mixing 90 wt% graphite powder with 10 wt% pre-prepared sodium carboxymethyl cellulose ($M_w \approx 250\,000$) binder solution (5 wt% in DI water). The slurries were well-mixed in a centrifugal mixer (Thinky, ARE-250 CE) for 10 min at 2000 rpm. The NMC811 cathode and graphite anode electrodes were then coated from slurries onto battery-grade Al and Cu foil, respectively. The coated electrodes were dried at 80 °C for 6 hours followed by vacuum drying for 24 hours. The 1.0 cm circular electrodes were cut, with the areal loading of the NMC811 cathodes ranging from 11 to 17 mg cm^{-2}, primarily due to differences in material characteristics, as all electrodes were coated under identical processing conditions. The average areal loadings of NMC-R1, NMC-R2, NMC-CS, and NMC-BASF electrodes were 12.9, 11.3, 16.7, and 15.2 mg cm^{-2}, respectively, with variations controlled within 4% across replicate samples. All electrodes were tested without calendering to evaluate the intrinsic electrochemical performance of the active materials under standard lab-scale conditions. Coin cells were then assembled inside a glovebox (H_2O < 0.5 ppm, O_2 < 0.5 ppm) using lithium metal (12 mm) as the counter electrode for half-cell tests, or graphite as the anode for full-cell tests with N/P ratios controlled between 1.05 and 1.15. The graphite electrodes were not pre-lithiated prior to assembly, consistent with standard commercial full-cell configurations in which the lithium inventory is provided exclusively by the cathode. The Whatman GF/A glass microfiber separator was saturated with 100 μL of 1 M $LiPF_6$ (EC/DMC, 1 : 1 by vol). Assembled cells were rested for 12 hours at room temperature before formation cycling to ensure electrolyte wetting. Three independent cells were tested to confirm reproducibility.

For NMC||Li half cells, long-term cycling experiments were performed at a rate of 0.33C within a voltage window of 3.0–4.2 V for 50 cycles. For high-loading coin cells, 50 cycles were conducted to differentiate electrode performance, assess cycling stability, and enable analysis of structural evolution. Prior to the cycling tests, two formation cycles were carried out at a rate of 0.05C between 3.0 and 4.2 V. For NMC||graphite full cells, three formation cycles were performed at a rate of 0.05C between 2.2 and 4.2 V. Rate capability testing was then carried out sequentially at 0.2C, 0.3C, 0.5C, 1C, and 2C, with each condition tested for 5 cycles, followed by cycling at 0.2C for an additional 50 cycles. All cycling measurements were conducted at 25 ± 1 °C using a LAND battery testing system with temperature controlled by a Neware environmental chamber. Electrochemical impedance spectroscopy (EIS) was conducted on NMC811||Li half cells over a frequency range of 1 MHz to 0.1 Hz with a signal height of 10.0 mV at room temperature before cycling and after discharging the cells to 3.0 V at the 50th cycle. Notably, the 1C rate was defined as 160 mA g^{-1} and applied consistently across all NMC811 samples in both half-cell and full-cell tests.

Results and discussion

Material characterisation

In the resynthesis of NMC811 cathodes, the precursor cathode active material (pCAM) was prepared using a conventional co-precipitation method. Two batches of leachate obtained from spent LIBs at a pilot-scale recycling facility were used to synthesise samples designated as NMC-R1 and NMC-R2. NMC-R2 was produced from a leachate that underwent an additional impurity removal step. A comparison sample was synthesised from high-purity (>99.9%) commercial metal sulphates under identical conditions (denoted as NMC-CS). A commercial NMC811 (denoted as NMC-BASF) was included for benchmarking purposes. As quantified by ICP-MS, NMC-R1 and NMC-R2 exhibited stoichiometries closest to the ideal 8 : 1 : 1 composition, whereas the CS and BASF samples contained comparable Ni content yet with higher Co and lower Mn contents (Table S1).

The industrial black mass used as feedstock in the recycling process contained Al (3.5 wt%), Cu (1.2 wt%), Fe (0.2 wt%), and other elements such as Ca, Mg, and Na (Table S2). The identity and content of impurities in the resynthesised and commercial NMC811 samples were further determined by ICP-MS and SEM-EDS analyses (Fig. 1). Cu, a potential impurity from the anode current collector, was absent in resynthesised NMC powders. Although Al was detected, its content remained sufficiently low at ~0.015% and was approximately the same in all samples including commercial NMC-BASF. These results confirm that current collector debris in LIB black mass can be effectively removed likely through physical separation or precipitation during the hydrometallurgical process, and Al or Cu are not the primary impurities of concern in resynthesised NMC cathodes. Trace amounts of Ca and Fe were detected only in NMC-R1 and

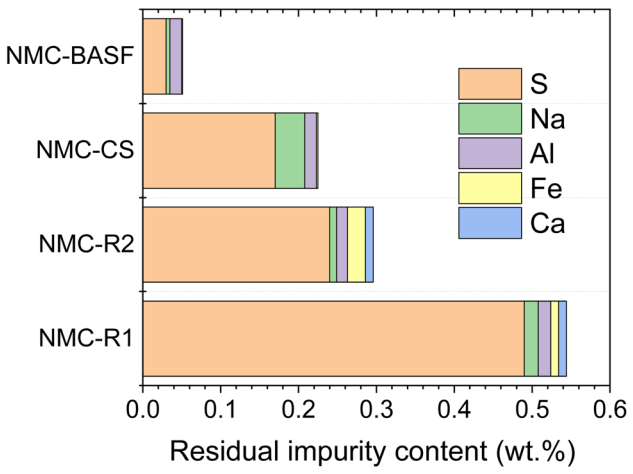

Fig. 1 The content of major impurities in commercial and resynthesised NMC811 samples.

NMC-R2. These persistent elements that are challenging for complete removal during recycling process reduce the overall purity of the final NMC811 products.

A significant amount of S was found in resynthesised samples with values of 0.49% for NMC-R1 and 0.24% for NMC-R2, in contrast to only 0.03% for NMC-BASF. NMC-CS sample synthesised using commercial metal salts, however, had only slightly lower S content (0.17%) than NMC-R1 and -R2. This indicates that co-precipitation, a process during which the dissolved metal sulphates form $NMC(OH)_2$ precipitate upon pH adjustment, would be the primary source of S impurity in final NMC powders.[30] In addition, due to the use of high-concentration sulphuric acid in the recycling process for metal leaching, the excess sulphate ions in the leachate could serve as another source of S impurities in resynthesised NMC.[14] Sulphate impurities in co-precipitated pCAM are known to be pH-dependent, with residual sulphur levels decreasing markedly above the point-of-zero-charge.[31] In the case of recovered metal precursors, the presence of excess sulphates and other impurities may interact with pCAM surfaces and modify surface charge characteristics, potentially shifting the effective point-of-zero-charge. Such shifts could alter sulphate adsorption–desorption equilibria during precipitation, reducing the efficiency of sulphur removal and contributing to the elevated residual sulphur content observed in the resynthesised NMC samples. Nevertheless, the purity of resynthesised NMC811 cathodes (99.65% for NMC-R2) exceeds the threshold of battery-grade cathode active materials, validating further detailed structure characterisation and performance evaluation.

Powder X-ray diffraction (PXRD) was used to elucidate the crystal structures and assess the structural integrity of various NMC811 samples. The diffraction patterns in Fig. 2 exhibited sharp, well-defined Bragg reflections characteristic of a single-phase layered structure with rhombohedral symmetry ($R\bar{3}m$ space group), consistent with the α-$NaFeO_2$-type structure.[32] No secondary phases were detected within the resolution limits of the diffractometer.

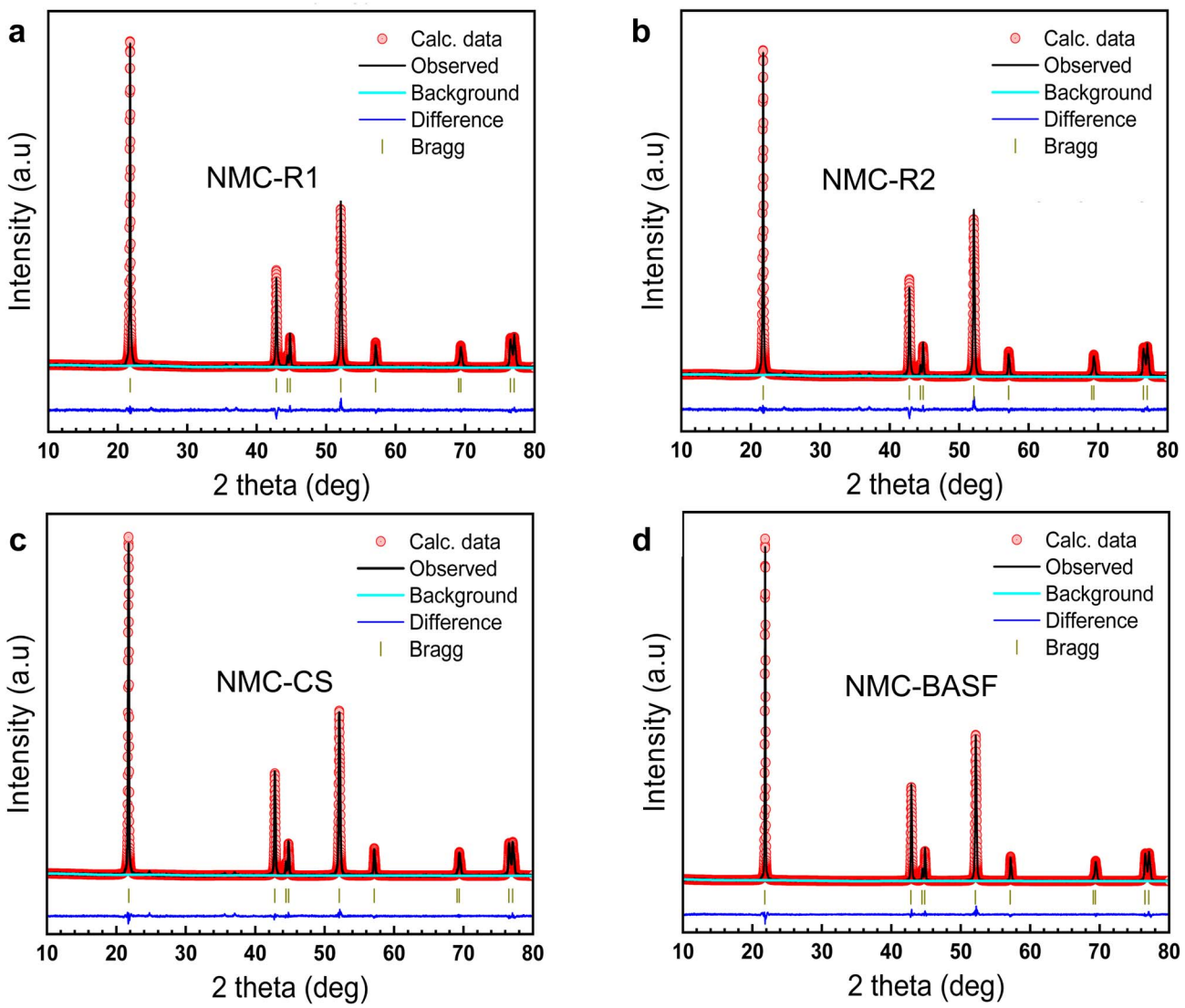

Fig. 2 Rietveld refinement pattern of PXRD data. (a) NMC-R1. (b) NMC-R2. (c) NMC-CS. (d) NMC-BASF.

Table 1 Rietveld refinement results of NMC811 samples

Sample	a/b (Å)	c (Å)	V (Å^3)	$I_{(003)}/I_{(104)}$	GOF	R_{wp} (%)	Li/Ni occupancy (%)
NMC-R1	2.870(2)	14.189(4)	101.30(2)	1.86	0.72	4.09	1.5(6)
NMC-R2	2.872(4)	14.20(3)	101.97(3)	1.87	0.69	4.0	0.98(4)
NMC-CS	2.875(2)	14.199(5)	101.45(5)	1.98	0.95	4.14	0.95(4)
NMC-BASF	2.871(2)	14.196(2)	101.37(1)	2.19	0.81	5.72	0.91(3)

To further evaluate deviations in the lattice parameters, PXRD data were subjected to Rietveld refinement (Table 1). A key parameter used to assess cation distribution within the crystal lattice of NMC811 materials is the intensity ratio of the (003) to (104) reflections, denoted as $I_{(003)}/I_{(104)}$.[33] This ratio serves as an indicator of cation mixing between Li and Ni ions, with higher values suggesting lower degrees of cation disorder.[34] The commercial NMC-BASF demonstrated the highest $I_{(003)}/I_{(104)}$ ratio of 2.19, indicative of minimal cation mixing and a well-ordered layered structure. By contrast, NMC-R1, which exhibited the lowest purity (99.41%) among all samples, showed a $I_{(003)}/I_{(104)}$ ratio of 1.86, a Li/Ni cation mixing of 1.5% and a reduced unit cell volume of 101.30(2) Å^3. Although $I_{(003)}/I_{(104)}$ values of NMC-R2 and -CS were still lower than NMC-BASF, their Li/Ni cation mixing was below 1%. This consistent trend between sample purity and structural integrity indicates the negative impacts of the residual impurity elements that destabilise the layered arrangement and promote the undesired nickel ion migration into lithium sites.

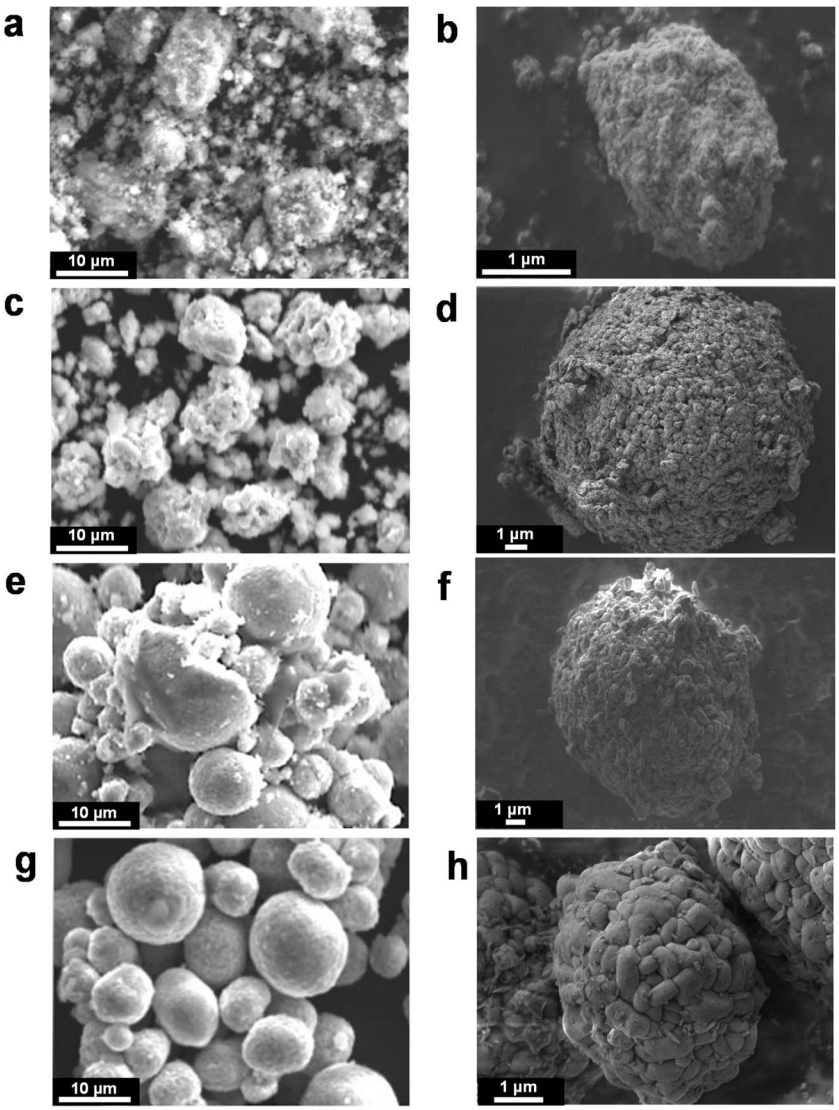

Fig. 3 SEM images of NMC811 samples. (a and b) NMC-R1. (c and d) NMC-R2. (e and f) NMC-CS. (g and h) NMC-BASF.

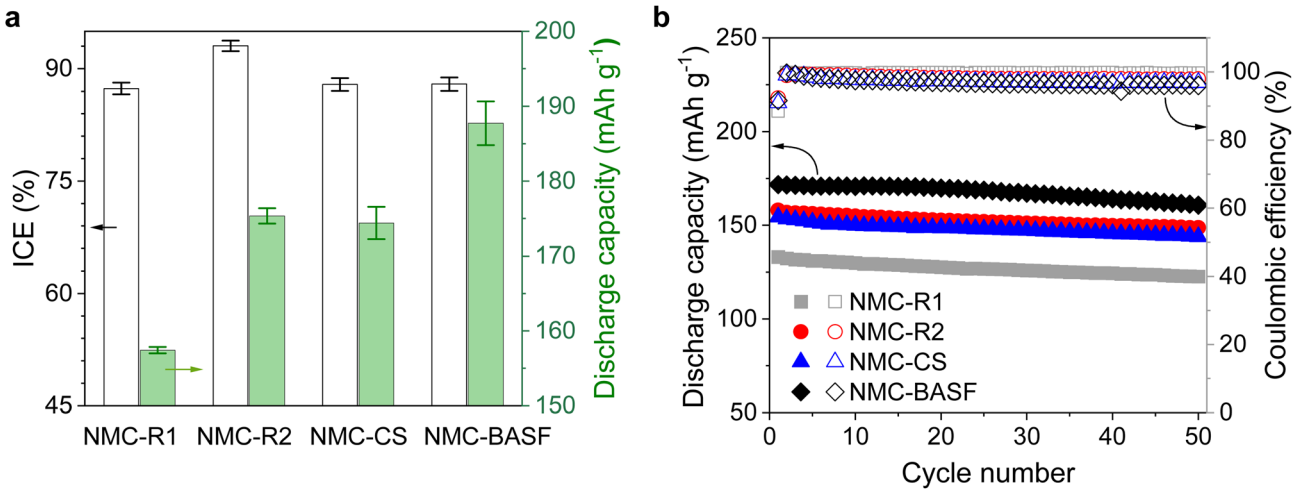

Fig. 4 Electrochemical performance of NMC811||Li half-cell measurements. (a) Summary of the ICEs and discharge capacities. Error bars represent standard deviation based on three independent cells. (b) Cycling performance at 0.33C. The 1C rate was defined as 160 mA g^{-1}.

The SEM images in Fig. 3 revealed distinct morphological differences among the NMC samples. NMC-R1 showed the most irregular morphology, consisting of loosely agglomerated secondary particles with non-uniform shapes and sizes. NMC-R2 displayed more defined secondary particles with partial sphericity, although the overall size distribution remains broad. In contrast, NMC-CS exhibited well-developed spherical secondary particles with improved size uniformity, closely resembling the morphology of the commercial NMC-BASF. Such compact and homogeneous structures are characteristic of high-quality cathode materials.

To complement the SEM observations, key physical properties of the NMC samples, including particle size distribution, skeletal and tapped densities, pH of water extract, and specific surface area, were measured (Table S3). NMC-R1 had the smallest particle size (D_{50} = 9.27 μm) and the lowest skeletal/tapped densities (3.43/2.53 g cm^{-3}), consistent with its irregular and loosely packed morphology. NMC-R2 had a larger median size (D_{50} = 12.70 μm), similar to NMC-CS and NMC-BASF, but showed the broadest distribution ($D_{90} - D_{10}$ = 16.86 μm) and relatively low skeletal/tapped densities (3.72/2.59 g cm^{-3}), indicating porous secondary particles with limited packing efficiency. In comparison, NMC-CS and NMC-BASF

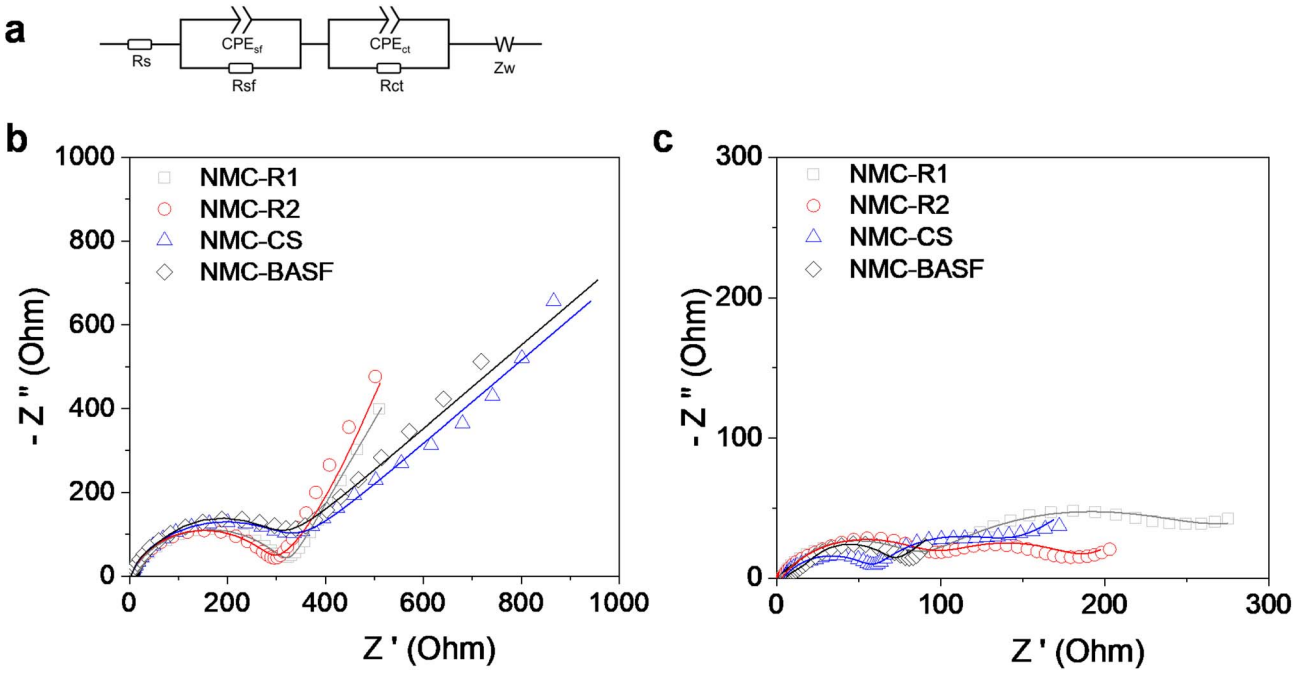

Fig. 5 Nyquist plots of EIS measurements and their fits at room temperature of NMC811||Li half cells. (a) Equivalent circuit model used for fitting. (b) Before cycling. (c) After 50 cycles at 0.33C. Fitted lines are overlaid on experiment data (symbols). The 1C rate was defined as 160 mA g^{-1}.

exhibited higher skeletal/tapped densities (4.10/2.67 and 4.26/2.89 g cm^{-3}, respectively) and narrower size distributions ($D_{90} - D_{10}$ = 14.05 and 11.35 μm, respectively), reflecting their uniform, well-packed secondary particles. The pH of the water extract was comparable for all samples (11.7–11.8), suggesting similar surface alkalinity. Overall, NMC-R2 demonstrated material properties approaching those of the commercial benchmark (NMC-BASF), although slight irregularities in particle shape and packing remained. These morphological characteristics directly influenced powder packing behaviour and density. As a result, NMC-CS and NMC-BASF, with their compact spherical particles, achieved higher tapped densities and more efficiently packed electrodes (15–16 mg cm^{-2}), whereas the irregular morphologies of NMC-R1 and NMC-R2 led to lower packing densities and reduced areal loadings (11–12 mg cm^{-2}).

Table 2 The fitted resistance values of EIS measurements

	Before cycling			After 50th cycles		
Sample	R_s (Ω)	R_{sf} (Ω)	R_{ct} (Ω)	R_s (Ω)	R_{sf} (Ω)	R_{ct} (Ω)
NMC-R1	2.56	22.09	318.1	3.37	194.4	79.48
NMC-R2	2.3	6.36	278.3	2.96	92.3	91.34
NMC-CS	2.32	58.56	224.9	4.19	55.2	75.58
NMC-BASF	2.68	41.21	205.3	5.04	16.84	42.74

We attribute the ill-defined morphology of NMC-R1 and -R2 to the presence of a range of impurity ions that interfere with particle nucleation and growth during the co-precipitation process for NMC811 hydroxide precursor formation. Sulphate can influence morphology *via* pH-dependent adsorption, which modifies crystal growth and particle structure.[31] Lee *et al.* reported that excess SO_4^{2-} ions can hinder the growth of primary particles and lead to reduced growth of secondary particles,

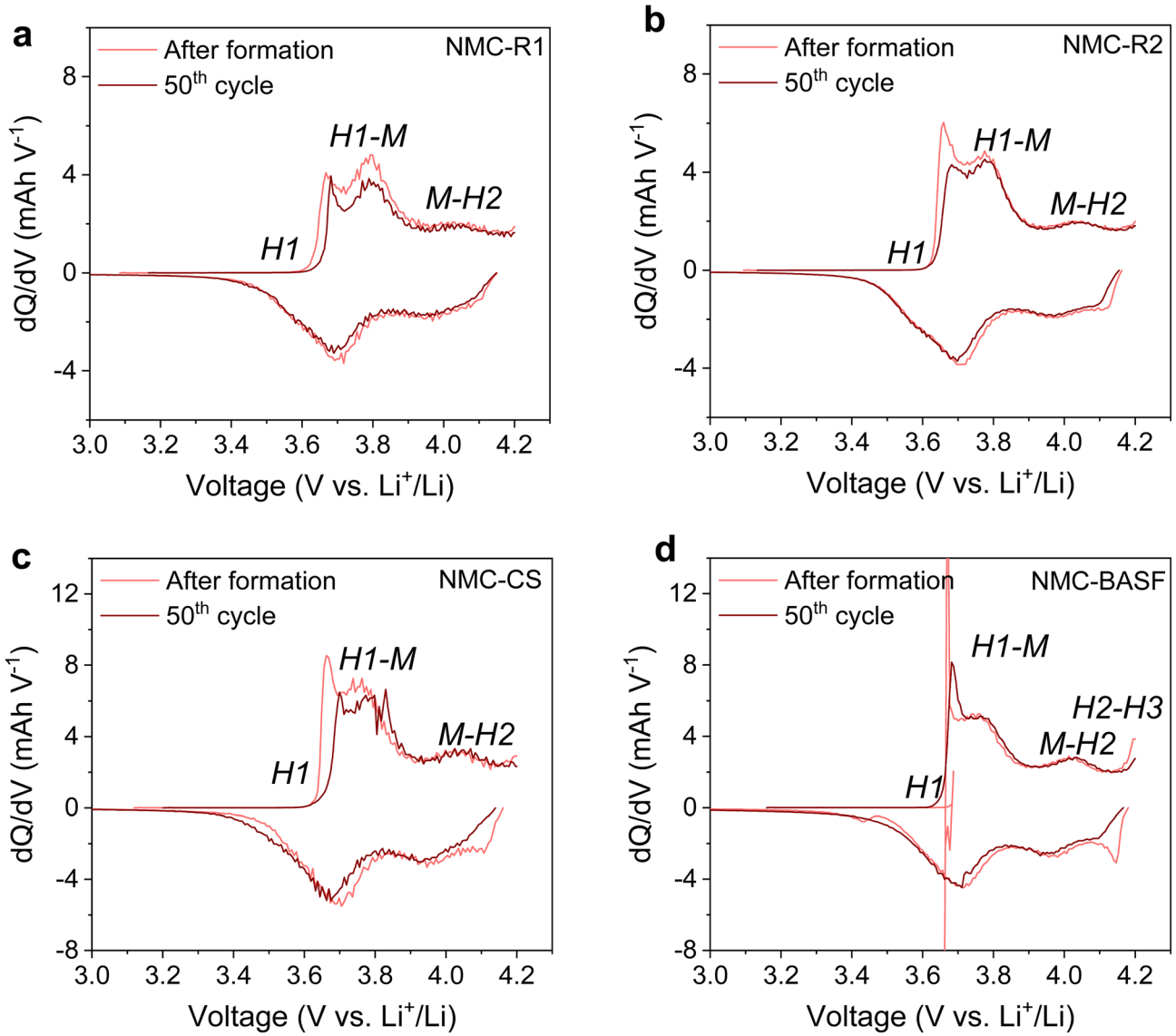

Fig. 6 Differential capacity plots of NMC811||Li half cells. (a) NMC-R1. (b) NMC-R2. (c) NMC-CS. (d) NMC-BASF.

yielding spherical but more porous secondary particles with smaller sizes compared to sulphate-free conditions.[14] Similarly, Fe^{2+}/Fe^{3+} ions can also promote the formation of sheet-like or porous primary particles, further leading to irregular secondary structures,[35] and Al^{3+} ions can inhibit crystal growth and result in smaller secondary particles with a broad size distribution.[12,36,37] These results indicate that interactions with residual impurities during pCAM synthesis can lead to morphological variations, which subsequently influence the properties of the final cathode material.

Electrochemical performance in NMC811||Li half cells

Fig. 4a summarises the average initial discharge capacities and initial coulombic efficiencies (ICEs) of NMC811||Li half cells during the first cycle at 0.05C within the voltage window of 3.0–4.2 V, with full statistical data provided in Table S4. The initial discharge specific capacities for NMC-R1, NMC-R2, NMC-CS, and NMC-BASF were 157.4, 175.3, 174.4, and 187.7 mAh g^{-1}, respectively, while the corresponding ICEs were 87.4%, 93.0%, 87.4%, and 88.0%, respectively. The lowest discharge capacity in NMC-R1 can be attributed to its higher degree of cation disorder, and ill-defined particle morphology. NMC-R2 exhibited the highest ICE (93.0%) among all samples, while also delivering a comparable discharge capacity to NMC-CS, the material synthesised from commercial-grade metal salts. The relatively lower ICEs of NMC-CS and NMC-BASF may result from their higher mass loadings, which can promote side reactions and limit lithium utilisation during the first cycle. A minor voltage-uptake feature was observed at the beginning of charge in NMC-CS (Fig. S1), which is characteristic of Ni-rich NMCs and typically arises from surface equilibration processes such as the oxidation of residual lithium species during the initial formation cycle.[38–41] This feature may possibly contribute to the slightly lower ICE but has no measurable effect on the subsequent electrochemical performance in our study. Nevertheless, both the initial capacity and ICEs of NMC-R2 fall within the range reported for resynthesised or regenerated NMC811 cathodes in the literature (Table S5), and the NMC-CS and commercial NMC-BASF also show values consistent with high-quality NMC811.[12,15,42–46]

To further evaluate their electrochemical performances, cycling tests (Fig. 4b) were conducted at a current rate of 0.33C. After 50 cycles, all samples demonstrated comparable capacity retention, with values of 92.1%, 94.1%, 93.2%, and 93.6% for NMC-R1, NMC-R2, NMC-CS, and NMC-BASF, respectively. Electrochemical impedance spectroscopy (EIS) was then performed to assess interfacial and charge-transfer characteristics during cycling. The Nyquist plots displayed a typical profile comprising two semicircles at high to medium frequencies and a sloped line at low frequencies (Fig. 5). The R_s specifies the ohmic resistance of the electrolyte solution. The first semicircle in the high-frequency region is attributed to the surface film resistance of the cathode–electrolyte interphase (R_{sf}), while the second semicircle in the medium-frequency region corresponds to the charge transfer-resistance (R_{ct}). The low-frequency tail is associated with the Warburg impedance, reflecting lithium-ion diffusion within the electrode material.[47,48]

All samples exhibited comparable impedance values before cycling, indicating consistent cell preparation (Table 2). After 50 cycles, NMC-R1 displayed the highest resistance, attributed to its disordered morphology, impurity enrichment, and partial cation disorder, which together hindered Li^+ transport.[49,50] In contrast, NMC-BASF maintained the lowest values for both R_{ct} (42.74 Ω) and R_{sf} (16.84 Ω), followed by NMC-CS, while NMC-R2 showed slightly higher resistance yet remained markedly lower than NMC-R1. These trends are consistent with the morphological characteristics observed before and after 50 cycles

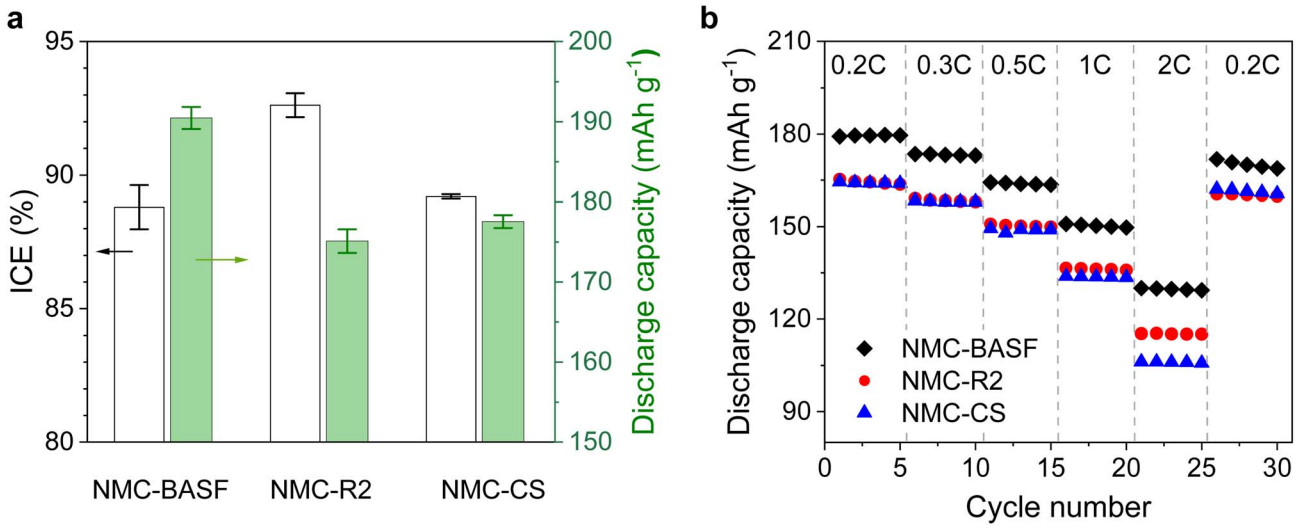

Fig. 7 Electrochemical performance of NMC811||graphite full-cell measurements. (a) Summary of the ICEs and charge capacities. Error bars represent standard deviation based on three independent cells (b) rate performance. The 1C rate was defined as 160 mA g^{-1} across all NMC811 samples. The average areal loadings of NMC-R1, NMC-R2, NMC-CS, and NMC-BASF electrodes were 12.9, 11.3, 16.7, and 15.2 mg cm^{-2}, respectively.

(Fig. S2 and S3), where more coherent and uniform particle structures were associated with greater interfacial stability. Hence, the EIS analysis highlights the combined influence of morphology and composition on the electrochemical behaviour of Ni-rich cathodes.[51]

Differential capacity plots were used to further analyse the redox behaviour and phase transitions (Fig. 6). These curves provide detailed information on the electrochemical processes occurring during lithium extraction and insertion. In Ni-rich cathodes such as NMC811, several distinct redox peaks are typically observed during charging. These peaks correspond to phase transitions from the initial hexagonal phase to a monoclinic structure, followed by further transformation to more lithium-deficient hexagonal phases (H1–M–H2–H3).[52,53] In this study, peak maxima were identified at ~3.65 V, 3.75 V, 3.9 V, and 4.2 V, consistent with previously reported values.[54] The H1–H2 region contributes the majority of the capacity, while the H2–H3 region provides only a limited capacity (<20 mAh g^{-1}).[55]

NMC-BASF exhibited sharp and well-defined redox peaks, indicating uniform phase evolution, low cation disorder, and excellent structural integrity. In contrast, NMC-R1, NMC-R2, and NMC-CS displayed broader and less distinct peaks, indicating greater heterogeneity in the local electrochemical environment. After 50 cycles, a minor shift of the redox peaks to higher potentials during charging and lower potentials during discharging was observed for all the samples except NMC-BASF, likely arising from increased interfacial resistances.[56] The negligible peak shifts observed for NMC-BASF aligned with its minimal impedance values. In addition, the onset of the H2–H3 phase transition in NMC-BASF occurred at a relatively lower voltage compared to the other samples, allowing it to access more high-voltage capacity and therefore deliver a higher discharge capacity.[57]

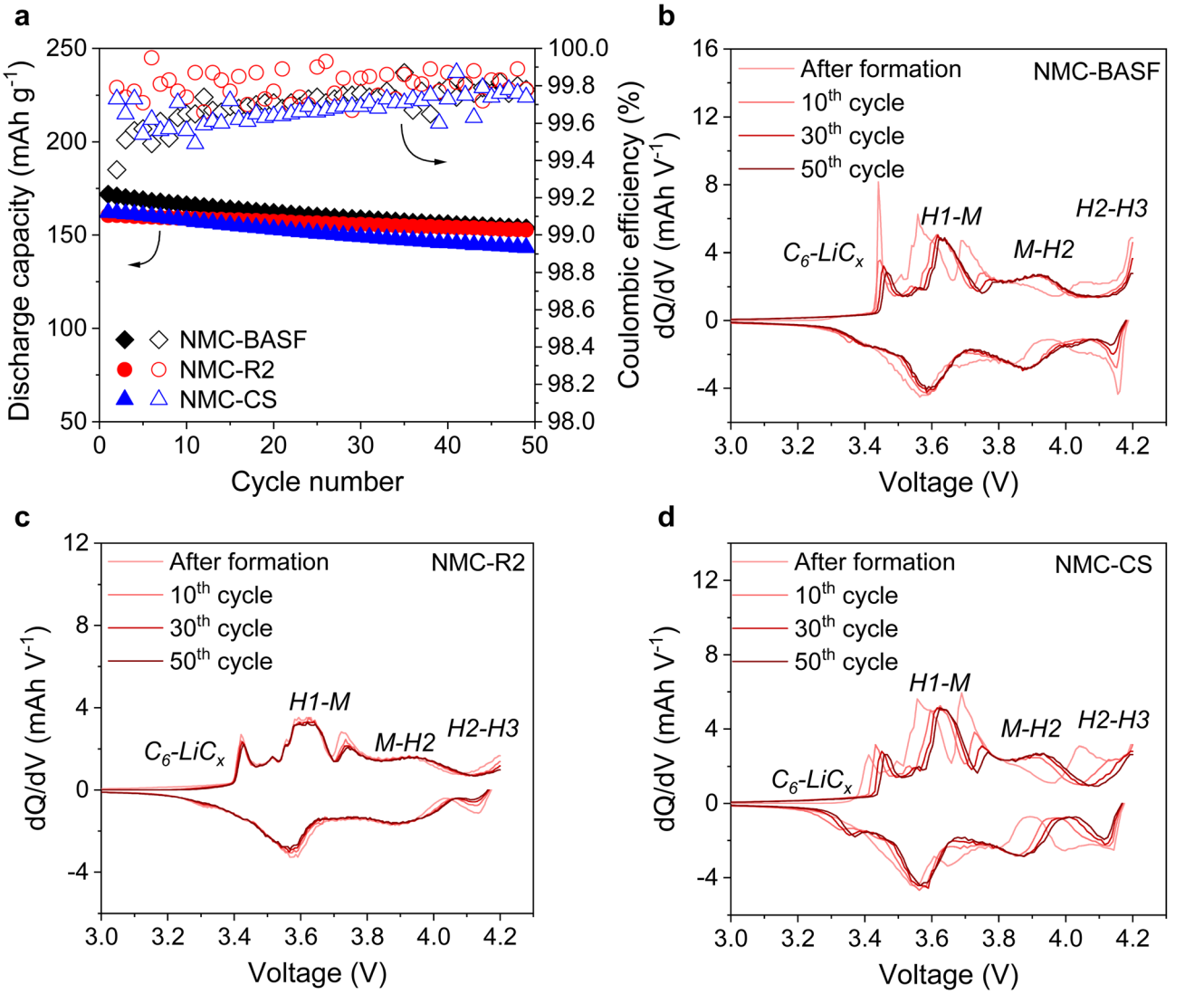

Fig. 8 (a) Cycling performance in NMC811||graphite full cells at 0.2 C. (b) dQ/dV plot of NMC-BASF. (c) dQ/dV plot of NMC-R2. (d) dQ/dV plot of NMC-CS. The 1C rate was defined as 160 mA g^{-1} across all NMC811 samples. The average areal loadings of NMC-R1, NMC-R2, NMC-CS, and NMC-BASF electrodes were 12.9, 11.3, 16.7, and 15.2 mg cm^{-2}, respectively.

Overall, NMC-R2 exhibited comparable capacity retention to NMC-BASF. However, its morphological differences may be associated with the higher interfacial resistances observed in EIS, and the slight peak shifts in the dQ/dV profiles indicate increased polarisation, which can in turn limit accessible capacity and affect long-term electrochemical kinetics. Consistent with this, extended 1C half-cell cycling (Fig. S4 and Table S6) showed that both NMC-BASF and NMC-R2 maintained ~95% capacity retention after 50 cycles, and decreased to 92.6% and 91.5%, respectively, after 100 cycles.

Electrochemical performance in NMC811||graphite full cells

Full cell tests were performed for three samples, *i.e.*, NMC-R2, NMC-CS and NMC-BASF, to further investigate the influence of precursor purity and particle morphology on battery performance. The performance trend observed in full cells was consistent with that in half-cell testing (Fig. 4 and 7). NMC-R2 and NMC-CS delivered initial discharge capacities of approximately 175.1 and 177.6 mAh g^{-1}, respectively, at a rate of 0.05C, slightly lower than that of NMC-BASF (190.5 mAh g^{-1}). The C-rate tests demonstrated that NMC-BASF maintained the highest discharge capacity across all tested current rates (Fig. 7b). Despite the differences in absolute discharge capacity, NMC-R2 and NMC-BASF exhibited comparable relative capacity retention across all C-rates (Fig. S5).

The cycling performance of NMC811||graphite full cells was evaluated over 50 cycles within a voltage window of 2.2–4.2 V (Fig. 8a). After 50 cycles, the specific discharge capacities reached 143.2 mAh g^{-1} for NMC-CS, 152.6 mAh g^{-1} for NMC-R2, and 153.5 mAh g^{-1} for NMC-BASF. The full cell based on NMC-R2 exhibited the highest capacity retention (95.1%), surpassing that of the cell using commercial NMC-BASF (89.3%).

In the full-cell dQ/dV plots (Fig. 8b–d), the H2–H3 phase transition of NMC-CS and NMC-BASF became more pronounced compared with the half-cell configuration, as the cathode experienced a higher effective potential in full cells. From the 10th to the 50th cycle, the redox peaks of NMC-CS and NMC-BASF shifted to higher potentials compared with NMC-R2, indicating increased polarisation in the full-cell configuration.[53] This behaviour contrasted with the half-cell measurements, where NMC-R2 exhibited higher resistance for both R_{sf} and R_{ct}. This evolution in the full cells could be attributed to accumulated lattice strain from the H2–H3 transition, alongside kinetic and transport limitations intrinsic to full cells. Accessing the H2–H3 region contributes to higher discharge capacity, but repeated cycling through this high-voltage transition is known to induce lattice strain and inter- and intra-granular microcracking, which can promote material degradation.[57–60] Evidence of microcrack formation in NMC-BASF (Fig. S6) is consistent with these observations. In contrast, NMC-R2 exhibited broader yet largely unshifted dQ/dV features and did not display a distinct H2–H3 peak within the tested voltage window, indicating greater kinetic heterogeneity but a less pronounced high-voltage phase-transition response. This may be partly attributed to its higher S content, as Savina *et al.* reported that sulphate-containing NMC811 exhibited smoother phase transitions and partial suppression of the H2–H3 transformation at high potentials, thereby mitigating structural degradation during cycling.[30] The slightly higher Mn content in NMC-R2 compared with NMC-CS and NMC-BASF may also play a role, as diffused Mn^{4+} at particle surfaces has been suggested to stabilise the structure and improve retention.[61] However, SEM images (Fig. S6) also showed signs of increased surface porosity in NMC-R2 after 50 cycles, which could allow greater electrolyte penetration and accelerate surface degradation upon further cycling. Therefore, although NMC-R2 showed encouraging electrochemical performance largely driven by its intrinsic structural features, its longer-term stability remains limited due to its suboptimal particle morphology. This indicates that further optimisation is required before undertaking extended lifespan evaluations.

Conclusion

This study provides a comprehensive assessment of NMC811 cathodes resynthesised from industrially recovered precursors, establishing the link between residual impurities, material crystallinity, morphology, and electrochemical performance. Although the resynthesised samples contained higher levels of impurities such as sulphur, sodium, and iron compared with commercial references, NMC-R2 achieved a purity of 99.6%, meeting the industrial threshold for battery-grade materials. NMC-R2 also delivered competitive half- and full-cell performance than both commercial cathodes and those synthesised from commercial metal salts. However, the findings indicate that impurities present in the recovered precursors had a notable impact on primary and secondary particle formation, resulting in broader particle size distributions and less compact morphologies.

From a sustainability perspective, life cycle assessment modelling (Tables S7 and S8) indicates that producing Ni-rich NMC cathodes from Altilium's recycled precursors can reduce cradle-to-gate greenhouse gas emissions by ~60% compared with mined raw materials, and by 22% and 39% relative to conventional hydro- and pyro-metallurgical recycling routes, respectively, with a further 20–25% reduction achievable using UK-based renewable electricity. These findings align with reported hydrometallurgical recycling reductions of 8–22%, and up to 49–54% under high secondary supply scenarios, indicating that our performance falls within or exceed the expected range for advanced recycling pathways when compared with primary production.[62]

Overall, this work demonstrates the feasibility of producing battery-grade NMC811 from recovered precursors while delivering strong environmental benefits. It also provides a clear basis for future optimisation of precursor processing and material engineering to support industrial scale-up.

Author contributions

XW: conceptualisation, methodology, data curation, validation, writing and review. MA, VS, BW and CM: CAM material

synthesis, SEM (Zeiss) and PXRD tests. AH: supervision, resources and review. MT: supervision, resources, funding acquisition and review.

Conflicts of interest

The authors declare no conflict of interest.

Data availability

The authors confirm that the data supporting the findings of this study are available within the article and its supplementary information (SI). Supplementary information is available. See DOI: https://doi.org/10.1039/d5ta06740e.

Raw data that support the findings of this study include proprietary information provided by Altilium Clean Technology through an industrial collaboration. Data can be shared upon reasonable request, subject to confidentiality constraints.

CCDC 2502959 contains the supplementary crystallographic data for this paper.[63]

Acknowledgements

XW, AH, CM and MT gratefully acknowledge funding from Innovate UK (CAMEV 10048761).

References

1 J. R. C. European Commission, *Raw Materials Information System – Critical and Strategic Materials*, https://rmis.jrc.ec.europa.eu/eu-critical-raw-materials, accessed 7 June 2025.
2 C. o. t. E. Union, *Critical Raw Materials – Infographic*, https://www.consilium.europa.eu/en/infographics/critical-raw-materials/, accessed 7 June 2025.
3 E. Commission, *Critical raw materials*, https://single-market-economy.ec.europa.eu/sectors/raw-materials/areas-specific-interest/critical-raw-materials_en, accessed 7 June 2025.
4 S. Jia, W. Meng and S. Li, *Sci. Rep.*, 2025, **15**, 10142.
5 Z. Meng, X. Ma, J. Hou, Y. Zheng and Y. Wang, *Adv. Energy Mater.*, 2025, e202405383.
6 Z. Meng, X. Ma, L. Azhari, J. Hou and Y. Wang, *Commun. Mater.*, 2023, **4**, 9.
7 S. Roy, H. Moustafa, K. Vaidya, J. P. Harvey and L. Fradette, *npj Energy Materials*, 2025, **3**, 15.
8 M. L. Machala, X. Chen, S. P. Bunke, G. Forbes, A. Yegizbay, J. A. de Chalendar, I. L. Azevedo, S. Benson and W. A. Tarpeh, *Nat. Commun.*, 2025, **16**, 988.
9 E. Union, *Sustainability rules for batteries and waste batteries*, https://eur-lex.europa.eu/EN/legal-content/summary/sustainability-rules-for-batteries-and-waste-batteries.html, accessed 7 June 2025.
10 Regulation (EU) 2023/1542 of the European Parliament and of the Council, *Off. J. Eur. Union*, 2023, **L191**, 1–117.
11 G. Harper, R. Sommerville, E. Kendrick, L. Driscoll, P. Slater, R. Stolkin, A. Walton, P. Christensen, O. Heidrich, S. Lambert, A. Abbott, K. Ryder, L. Gaines and P. Anderson, *Nature*, 2019, **575**, 75–86.
12 R. Zhang, Y. Zheng, Z. Yao, P. Vanaphuti, X. Ma, S. Bong, M. Chen, Y. Liu, F. Cheng, Z. Yang and Y. Wang, *ACS Sustain. Chem. Eng.*, 2020, **8**, 9875–9884.
13 X. Wei, Z. Guo, Y. Zhao, Y. Sun, A. Hankin and M. Titirici, *RSC Sustain.*, 2024, **3**, 264–274.
14 J. Lee, S. Park, M. Beak, S. R. Park, A. R. Lee, S. H. Byun, J. Song, J. S. Sohn and K. Kwon, *Materials*, 2021, **14**, 6672.
15 M. Beak, S. Park, S. Kim, J. Park, S. Jeong, B. Thirumalraj, G. Jeong, T. Kim and K. Kwon, *J. Alloys Compd.*, 2021, **873**, 159808.
16 Q. Sa, J. A. Heelan, Y. Lu, D. Apelian and Y. Wang, *ACS Appl. Mater. Interfaces*, 2015, **7**, 20585–20590.
17 S. Park, D. Kim, H. Ku, M. Jo, S. Kim, J. Song, J. Yu and K. Kwon, *Electrochim. Acta*, 2019, **296**, 814–822.
18 Y. Weng, S. Xu, G. Huang and C. Jiang, *J. Hazard. Mater.*, 2013, **246–247**, 163–172.
19 O. A. Nasser and M. Petranikova, *Batteries*, 2021, **7**, 60.
20 M. Beak, J. Park, S. Park, S. Jeong, J. Kang, W. Choi, W. S. Yoon and K. Kwon, *J. Hazard. Mater.*, 2022, **425**, 127907.
21 R. Zhang, Z. Meng, X. Ma, M. Chen, B. Chen, Y. Zheng, Z. Yao, P. Vanaphuti, S. Bong, Z. Yang and Y. Wang, *Nano Energy*, 2020, **78**, 105214.
22 P. Hou, J. Yin, M. Ding, J. Huang and X. Xu, *Small*, 2017, **13**, 1701802.
23 S. Jamil, G. Wang, L. Yang, X. Xie, S. Cao, H. Liu, B. Chang and X. Wang, *J. Mater. Chem. A*, 2020, **8**, 21306–21316.
24 C. Xu, K. Marker, J. Lee, A. Mahadevegowda, P. J. Reeves, S. J. Day, M. F. Groh, S. P. Emge, C. Ducati, B. Layla Mehdi, C. C. Tang and C. P. Grey, *Nat. Mater.*, 2021, **20**, 84–92.
25 J. Park, S. Park, M. Beak, S. Jeong and K. Kwon, *J. Cleaner Prod.*, 2022, **379**, 134570.
26 T. Entwistle, E. Sanchez-Perez, G. J. Murray, N. Anthonisamy and S. A. Cussen, *Energy Rep.*, 2022, **8**, 67–73.
27 R. Jung, M. Metzger, F. Maglia, C. Stinner and H. A. Gasteiger, *J. Phys. Chem. Lett.*, 2017, **8**, 4820–4825.
28 H. M. Rietveld, *J. Appl. Crystallogr.*, 1969, **2**, 65–71.
29 H. M. Rietveld, *Acta Crystallogr.*, 1967, **22**, 151–152.
30 A. A. Savina, E. D. Orlova, A. V. Morozov, S. Y. Luchkin and A. M. Abakumov, *Nanomaterials*, 2020, **10**, 2381.
31 R. B. Berk, T. Beierling, L. Metzger and H. A. Gasteiger, *J. Electrochem. Soc.*, 2023, **170**, 110513.
32 W. Lee, S. Muhammad, T. Kim, H. Kim, E. Lee, M. Jeong, S. Son, J. H. Ryou and W. S. Yoon, *Adv. Energy Mater.*, 2018, **8**, 1701788.
33 W. El Mofid, S. Ivanov, A. Konkin and A. Bund, *J. Power Sources*, 2014, **268**, 414–422.
34 X. Zhang, W. J. Jiang, A. Mauger, L. Qi, F. Gendron and C. M. Julien, *J. Power Sources*, 2010, **195**, 1292–1301.
35 R. Zhang, Y. Zheng, P. Vanaphuti, Y. Liu, J. Fu, Z. Yao, X. Ma, M. Chen, Z. Yang, Y. Lin, J. Wen and Y. Wang, *ACS Appl. Energy Mater.*, 2021, **4**, 10356–10367.
36 Y. Wang and Y. Zheng, *ECS Meeting Abstracts*, 2022, **5**, 590.

37 S. Kim, S. Park, M. Jo, M. Beak, J. Park, G. Jeong, J. S. Yu and K. Kwon, *J. Alloys Compd.*, 2021, **857**, 157581.
38 M. Su, Y. Chen, H. Liu, J. Li, K. Fu, Y. Zhou, A. Dou and Y. Liu, *Electrochim. Acta*, 2022, **422**, 140559.
39 R. Jung, R. Morasch, P. Karayaylali, K. Phillips, F. Maglia, C. Stinner, Y. Shao-Horn and H. A. Gasteiger, *J. Electrochem. Soc.*, 2018, **165**, A132.
40 C. Lv, Z. Li, X. Ren, K. Li, J. Ma and X. Duan, *J. Mater. Chem. A*, 2021, **9**, 3995–4006.
41 I. De Meatza, I. Landa-Medrano, S. Sananes-Israel, A. Eguia-Barrio, O. Bondarchuk, S. Lijó-Pando, I. Boyano, *et al.*, *Batteries*, 2022, **8**, 79.
42 Z. Qin, T. Zhang, X. Gao, W. Luo, J. Han, B. Lu, J. Zhou and G. Chen, *Adv. Mater.*, 2024, **36**, e2307091.
43 P. Tammawat, T. Sesuk, P. Eiamlamai, P. Limthongkul and N. Kunanusont, *J. Power Sources*, 2025, **641**, 236827.
44 T. Wu, G. Wang, B. Liu, Q. Huang, Y. Su, F. Wu and R. M. Kelly, *J. Power Sources*, 2021, **494**, 229774.
45 M. Chen, Z. Zheng, Q. Wang, Y. Zhang, X. Ma, C. Shen, D. Xu, J. Liu, Y. Liu, P. Gionet, I. O'Connor, L. Pinnell, J. Wang, E. Gratz, R. Arsenault and Y. Wang, *Sci. Rep.*, 2019, **9**, 1654.
46 A. A. Savina and A. M. Abakumov, *Heliyon*, 2023, **9**, e21881.
47 J. Chen, H. Yang, T. Li, C. Liu, H. Tong, J. Chen, Z. Liu, L. Xia, Z. Chen, J. Duan and L. Li, *Front. Chem.*, 2019, **7**, 500.
48 I. Anconina and D. Golodnitsky, *RSC Appl. Interfaces*, 2025, **2**, 261–278.
49 J. Li, Z. Zhou, Z. Luo, Z. He, J. Zheng, Y. Li, J. Mao and K. Dai, *Sustainable Mater. Technol.*, 2021, **29**, e00305.
50 M. Jiang, D. L. Danilov, R.-A. Eichel and P. H. L. Notten, *Adv. Energy Mater.*, 2021, **11**, 2103005.
51 E. Laakso, S. Efimova, M. Colalongo, P. Kauranen, K. Lahtinen, E. Napolitano, V. Ruiz, J. Moškon, M. Gaberšček, J. Park and S. Seitz, *J. Power Sources*, 2024, **599**, 234159.
52 Y. Gao, J. Park and X. Liang, *ACS Appl. Energy Mater.*, 2020, **3**, 8978–8987.
53 G. Nuroldayeva, D. Adair, Z. Bakenov and B. Uzakbaiuly, *ACS Omega*, 2023, **8**, 37899–37907.
54 J. Li, L. E. Downie, L. Ma, W. Qiu and J. R. Dahn, *J. Electrochem. Soc.*, 2015, **162**, A1401–A1408.
55 K. Märker, P. J. Reeves, C. Xu, K. J. Griffith and C. P. Grey, *Chem. Mater.*, 2019, **31**, 2545–2554.
56 J. Choi, L. Dong, C.-Y. Yu, C. O'Meara, E. Lee and J.-H. Kim, *J. Electrochem. Energy Convers. Storage*, 2021, **18**, 041009.
57 T. Liu, L. Yu, J. Lu, T. Zhou, X. Huang, Z. Cai, A. Dai, J. Gim, Y. Ren, X. Xiao, M. V. Holt, Y. S. Chu, I. Arslan, J. Wen and K. Amine, *Nat. Commun.*, 2021, **12**, 6024.
58 F. Schipper, E. M. Erickson, C. Erk, J.-Y. Shin, F. F. Chesneau and D. Aurbach, *J. Electrochem. Soc.*, 2016, **164**, A6220–A6228.
59 J. Xu, E. Hu, D. Nordlund, A. Mehta, S. N. Ehrlich, X. Q. Yang and W. Tong, *ACS Appl. Mater. Interfaces*, 2016, **8**, 31677–31683.
60 H.-H. Ryu, K.-J. Park, C. S. Yoon and Y.-K. Sun, *Chem. Mater.*, 2018, **30**, 1155–1163.
61 T. Li, X.-Z. Yuan, L. Zhang, D. Song, K. Shi and C. Bock, *Electrochem. Energy Rev.*, 2020, **3**, 43–80.
62 J. A. Llamas-Orozco, F. Meng, G. S. Walker, A. F. N. Abdul-Manan, H. L. MacLean, I. D. Posen and J. McKechnie, *PNAS Nexus*, 2023, **2**, pgad361.
63 CCDC 2502959: Experimental Crystal Structure Determination, 2025, DOI: 10.25505/fiz.icsd.cc2q0jmx.

